Soft Matter

PAPER

View Article Online
View Journal | View Issue

Cite this: *Soft Matter*, 2025, **21**, 8140

Capillary and priming pressures control the penetration of yield-stress fluids through non-wetting 2D meshes

Manon Bourgade,[ab] Nicolas Bain,[a] Loïc Vanel,[a] Mathieu Leocmach[a] and Catherine Barentin*[a]

Received 25th July 2025,
Accepted 17th September 2025

DOI: 10.1039/d5sm00759c

rsc.li/soft-matter-journal

Forcing hydrophilic fluids through hydrophobic porous solids is a recurrent industrial challenge. If the penetrating fluid is Newtonian, the imposed pressure has to overcome the capillary pressure at the fluid–air interface in a pore. The presence of a yield-stress, however, makes the pressure transfer and the penetration significantly more complex. In this study, we experimentally investigate the forced penetration of a water based yield-stress fluid through a regular hydrophobic mesh under quasi-static conditions, combining quantitative pressure measurements and direct visualisation of the penetration process. We reveal that the penetration is controlled by a competition between the yield-stress and two distinct pressures: the capillary pressure, which dictates the threshold at which the yield-stress fluid penetrates the hydrophobic mesh, and a priming pressure, which controls how the fluid advances through it. The latter corresponds to a pressure drop ensuing a local capillary instability, never reported before. Our findings shed new light on forced imbibition processes, with direct implications on their fundamental understanding and practical engineering.

1. Introduction

We all intuitively know how to force a fluid into a porous medium. Take a sponge for instance and use it to wipe some fluid off a surface. Depending on whether the sponge is dry or not, with small or large pores, and whether that fluid is water, oil, or some thick sauce, we apply different pressures for absorption. In other words, the pore geometry, the fluid rheology, and its capillary affinity with the porous media all matter. When the medium is fully saturated with liquid, Darcy's law describes the viscous resistance against a forced flow. In this case, the flow rate is proportional to the applied pressure difference. When the porous medium is not saturated, capillarity kicks in. If the fluid wets the medium, it is spontaneously absorbed by it.[1] If it does not wet the medium, the capillary pressure at the fluid–air interface acts as a threshold pressure that must be overcome to observe any flow.[2–5] Such capillary constraints lead to a penetration behaviour much more intricate than the steady-state Darcy's flow.[2–5] When the fluid has a non-Newtonian rheology, the penetration behaviour is even more complex and remains scarcely investigated.

Out of the kitchen, however, the forced imbibition of non-Newtonian fluids into porous media is crucial for many practical applications, including filtration, textile processing and washing, or civil engineering. In particular, water-based yield-stress fluids[6] such as pastes, polymeric or colloidal gels represent many everyday fluids and are ubiquitous in the industrial context. The control of their penetration inside hydrophobic porous media, *e.g.* filters, fabric, skin or construction materials is a recurrent issue.

In wetting situations, the spontaneous imbibition of porous media by Newtonian fluids has been an active topic for a long time.[7] Capillary absorption or water transport by textiles has been widely studied, and in particular the role of liquid saturation,[8] porosity scales,[9] contact angles[10] and geometric details.[11] When it comes to yield-stress fluids, experimental and numerical investigations of the forced flow into homogeneously filled porous and fibrous media showed a behavior consistent with modified Darcy's law, where the yield stress induces another threshold pressure below which the fluid does not flow.[12–16] This threshold pressure induced by yield stress, different in nature from the capillarity induced one, was also observed in falling drop experiments.[17]

In non-wetting situations, the study of forced penetration has been limited to Newtonian fluids. It has been investigated both at a single pore level,[18,19] and in fiber layers,[20] either by falling drop experiments[18,21–25] or by static pressures.[18,20] In all cases the existence of a capillary threshold pressure was evidenced, influenced by geometry, below which penetration did

---

[a] *Universite Claude Bernard Lyon 1, CNRS, Institut Lumière Matière, UMR5306, F-69100, Villeurbanne, France. E-mail: catherine.barentin@univ-lyon1.fr*
[b] *Saint-Gobain Recherche Paris, 39 Quai Lucien Lefranc, 93300 Aubervilliers, France*

not occur. The forced penetration of yield-stress fluids, and how yield stress combines with the capillary threshold pressure, therefore remain unexplored.

In this study, we address this challenge by experimentally investigating the penetration behaviour of a water-based yield-stress fluid into a hydrophobic fibrous mesh with a quasi-static forced imbibition setup. After presenting our experimental setup, we first report measurements of the threshold penetration pressure required for a yield-stress fluid to pass through a hydrophobic mesh. We show that in the range of parameters we explore the threshold penetration pressure is dictated by the capillary pressure and has little dependence on the yield stress. We then focus on the local penetration phenomenology. In stark contrast, we show through detailed observation and modeling that the yield stress has a profound impact on the microscopic instabilities that govern the penetration path.

2. Experimental setup

2.1. Quasi-static forced imbibition

We illustrate our quasi-static forced imbibition setup in Fig. 1. We fill a syringe with a model yield-stress fluid. At one end of the syringe, we glue a hydrophobic mesh (see Section S1 for details). At the other end, we connect an air compressor that applies a controlled pressure P_0. This leads to a pressure at the mesh interface $P_{\mathrm{mesh}} = P_0 + \Delta P_{\mathrm{h}} - \Delta P_y$, where ΔP_{h} is the hydrostatic pressure and ΔP_y the contribution of the yield-stress fluid in the syringe (see Section S2 for details). In each measurement, we increase the applied pressure until the fluid flows through the mesh (see Section S3 for detailed experimental steps).

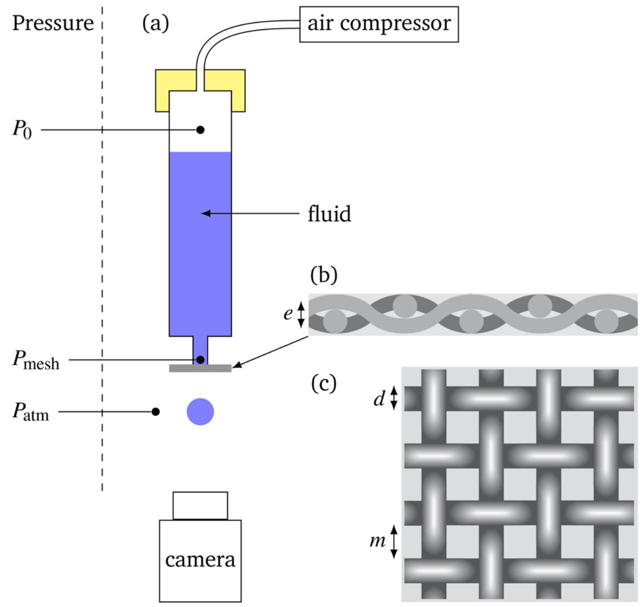

Fig. 1 (a) Quasi-static experimental setup. (b) and (c) Side-view and top-view diagrams, respectively, of the woven polyamide meshes (diagrams provided by the manufacturer). Definition of key dimensions: pore size *m*, fiber diameter *d*, and mesh thickness *e*.

We used an MFCS (microfluidic flow control system) air compressor from Fluigent, that can impose a pressure $P_0 = P_{\mathrm{atm}} + \Delta P_{\mathrm{comp}}$, where ΔP_{comp} ranges from 0 to 6900 Pa with a 2.5% precision. We manually increase this pressure using the software provided by the manufacturer, with increments of 2 Pa at each step, at a slow rate of about 10 Pa s^{-1} to keep the flow quasi-static.

2.2. Model yield stress fluids and 2D meshes

For the model yield-stress fluid,[26] we chose an aqueous suspension of Carbopol polymer microgels (Ultrez 10 powder) from Lubrizol[27] (see Section S4 for preparation protocol). For polymer concentrations above the jamming threshold $c^* \approx 0.09\%$ w/w, the suspension exhibits a yield stress resulting from the jamming of the microgels, whereas below c^* the suspension has no yield stress. To characterize the mechanical properties of the suspensions, we measure the flow curve using a rheometer (Anton Paar Physica MCR 302) with a parallel-plate geometry and determine the yield stress σ_y by fitting the data to a Herschel–Bulkley model (see Section S5). For polymer concentrations ranging from 0.1% w/w to 1.2% w/w, the yield stress σ_y varies from 4.4 Pa to 86 Pa ± 10%.

As for the hydrophobic meshes, we selected single layer meshes of woven polyamide fibers (SEFAR), with a well-controlled and uniform pore size *m*, fiber diameter *d*, and mesh thickness *e* (Fig. 1b and c). The manufacturer-provided dimensions are given in Table 1, and the corresponding references in Table S1.

To verify the hydrophobicity of the meshes, we placed water drops on their surface and measured macroscopic contact angles using a side camera and the Dropsnake module in ImageJ.[28] Measurements from four different drops give a super-hydrophobic average contact angle of 130°. In addition, we performed contact angle measurements on individual fibers, for which we estimated a contact angle ranging between 90° and 100° (see Section S6 for details).

2.3. Penetration visualisation

We visualise the fluid–air interface using a ZEISS Axio Zoom V16 microscope placed underneath the quasi-static compression setup (Fig. 1a). This system, capable of magnifying up to 112×, will be referred to as a macroscope hereafter. We used it to quantify the true pore size of the hydrophobic meshes m_{real} (Table 1), and to record videos of the fluid–air interface throughout the experiments. We illuminate the fluid–air interface with a ring light, and conveniently exploit its reflection

Table 1 Hydrophobic mesh geometric properties. The pore size *m*, fiber diameter *d* and mesh thickness *e* are defined in Fig. 1, and their values provided by the manufacturer. The true pore size m_{real} corresponds to the value we measured with the macroscope

Mesh #	m (μm)	d (μm)	e (μm)	m_{real} (μm)
1	64	33	50	71 ± 2.5
2	85	24	40	84 ± 1.5
3	105	40	63	104 ± 2.1
4	125	62	100	118 ± 2.3
5	190	62	100	177 ± 1.5

pattern to follow the progression of the fluid through the pores (Fig. 2). A typical experiment goes as follows. As we increase the applied pressure, the fluid approaches, contacts, and progressively flows through the mesh (Fig. 2a–d), until it protrudes from it (Fig. 2e and f). Following the first drop coalescence (Fig. 2g), we maintain a constant pressure. Subsequent fusions occur rapidly in less than 1 s (Fig. 2g–j) resulting in a connected cluster (Fig. 2j), and eventually passage of the fluid through the mesh.

Informed by this phenomenology, we define the penetration pressure ΔP_{pen} as the difference between the pressure applied by the compressor at the moment of the first coalescence event (Fig. 2g) and the one at which the fluid is brought in contact with the mesh (Fig. 2b). Experimentally, we measure it as $\Delta P_{\text{pen}} = \Delta P_{\text{coalescence}} - \Delta P_{\text{contact}}$.

3. Results and discussion

3.1. The penetration pressure is set by capillarity

3.1.1. Penetration pressure for a Newtonian fluid. We first consider the simpler case of a Newtonian fluid, in the absence of yield stress. Once the fluid contacts the mesh, the local curvature of the liquid–air interface in each pore gives rise to a pressure jump, the Laplace pressure ΔP_{L}. For a square pore formed by cylindrical fibers,[20]

$$\Delta P_{\text{L}}(\alpha) = -4\frac{\Gamma \sin(\alpha + \theta)}{m + \ell(1 - \sin\alpha)}, \qquad (1)$$

where α is the immersion angle along the fiber, Γ the surface tension of the fluid–air interface, θ the fluid-fiber contact angle, m the pore size, and ℓ the pore depth (Fig. 3 inset).

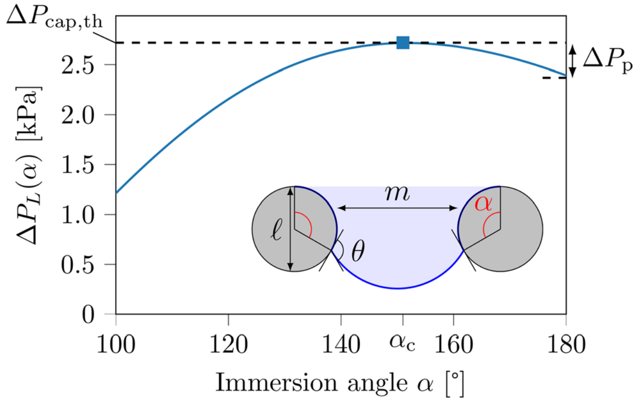

Fig. 3 Main: Laplace pressure as a function of the immersion angle α, for θ = 90°, m = 71 μm and ℓ = 33 μm. The maximum pressure $\Delta P_{\text{L,max}}$ is reached at the critical immersion angle α_{c}. The priming pressure ΔP_{p} is defined as $\Delta P_{\text{p}} = \Delta P_{\text{L,max}} - \Delta P_{\text{L}}(180°)$. Inset: definition of the parameters. α is the immersion angle, θ is the contact angle on a single fiber, m the pore size, ℓ the pore depth.

The Laplace pressure $\Delta P_{\text{L}}(\alpha)$ defined in eqn (1) has a non-monotonic behavior with the immersion angle α (Fig. 3). Advancing the meniscus through the pore first increases the Laplace pressure, until it reaches a maximum at a critical immersion angle α_{c}. Then, the meniscus can progress spontaneously through the pore, without any further pressure increase. We therefore expect the pressure at which a Newtonian fluid penetrates the mesh ΔP_{pen} to equate the maximal Laplace pressure $\Delta P_{\text{L,max}} = \Delta P_{\text{L}}(\alpha_{\text{c}})$.

To test this hypothesis, we carried out forced imbibition experiments for five mesh geometries and two fluids without

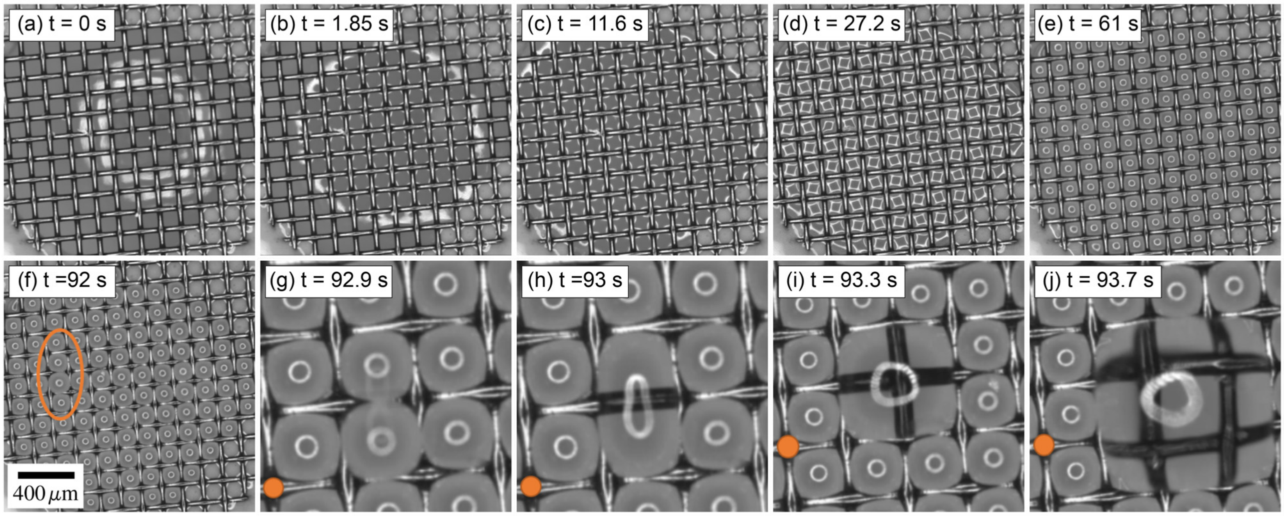

Fig. 2 Snapshots from an experiment with mesh 3 and a fluid with a yield stress of 66 Pa, showing the progression of the fluid–air interface. The camera focus is on the hydrophobic mesh, for which we can observe some side pores filled with glue. (a) The fluid approaches the mesh. The ring light forms a central circular reflection on the fluid front. (b) The fluid contacts the mesh at the center. The pores here show a small white reflection at the edges, indicating initial contact. At this step, the compressor pressure is $\Delta P_{\text{comp}} = \Delta P_{\text{contact}}$, the initial flowing pressure required to bring the yield stress fluid to the tip of the syringe. (c) The fluid contacts the entire mesh. (d) The fluid starts to advance into the pores, as the light reflections shift to square shapes in the pore centers. (e) The fluid lightly protrudes through the pores, forming circular reflection patterns. (f) As we increase the applied pressure, drops expand through the pores, nearing neighboring drops. The circled area indicates where the first breakthrough will occur. (g) Neighbouring drops touch and begin coalescing, accelerating the dynamics. (h)–(j) Successive coalescences quickly connect multiple pores, forming clusters as the fluid penetrates.

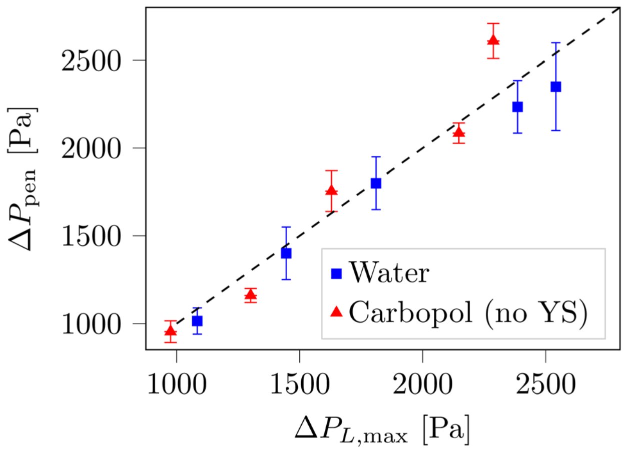

Fig. 4 Experimentally measured penetration pressure ΔP_{pen} as a function of theoretical maximum Laplace pressure $\Delta P_{\mathrm{L,max}}$, obtained with water (blue squares) and dilute Carbopol suspension without yield stress (red triangles). The symbol positions correspond to the mean value measured for at least 4 measurements in each condition, and the height of the error bars to the associated standard deviation. The dotted line corresponds to $\Delta P_{\mathrm{pen}} = \Delta P_{\mathrm{L,max}}$.

yield stress: water, and a dilute Carbopol suspension ($c = 0.05\%$ w/w $< c^*$). In each case, we compare the experimentally measured penetration pressure ΔP_{pen} against the maximal Laplace pressure $\Delta P_{\mathrm{L,max}}$, obtained from eqn (1) using $\Gamma = 72$ mN m^{-1} for water, $\Gamma = 63$ mN m^{-1} for Carbopol suspensions,[29,30] $\theta = 90°$, $m = m_{\mathrm{real}}$ and $\ell = e$ (Fig. 4). The good overall agreement between the experimental and theoretical values confirms that, in the absence of yield-stress, the penetration of a fluid through a hydrophobic woven mesh is entirely determined by capillarity.

3.1.2. Penetration pressure for a yield-stress fluid. We now turn to the effect of yield-stress. To this end, we performed quasi-static forced imbibition experiments for Carbopol solutions with yield-stress σ_y ranging from 0 to 85 Pa, through five mesh geometries, and systematically measured the penetration pressure ΔP_{pen} (Fig. 5). The measurements at $\sigma_y = 0$ Pa correspond to the ones presented above for a dilute Carbopol suspension (Fig. 4).

We first note that the penetration pressure mostly depends on the mesh geometry. The smaller the pore size, the larger the penetration pressure. More precisely, the major difference between any two geometries seems to be largely explained by the behavior in the absence of yield stress, at $\sigma_y = 0$ Pa, where the penetration is governed by the Laplace pressure $\Delta P_{\mathrm{L,max}}$. This observation suggests that we can separate the penetration pressure into a capillary and a yield-stress contribution,

$$\Delta P_{\mathrm{pen}} = \Delta P_{\mathrm{L,max}} + \Delta P_{\sigma_y}. \qquad (2)$$

In this case, we estimate from modified Darcy's law, the additional pressure required to make a yield-stress fluid flow through a pore of length e and diameter m_{real} is,[12,13]

$$\Delta P_{\sigma_y} = \beta \frac{e}{m_{\mathrm{real}}} \sigma_y, \qquad (3)$$

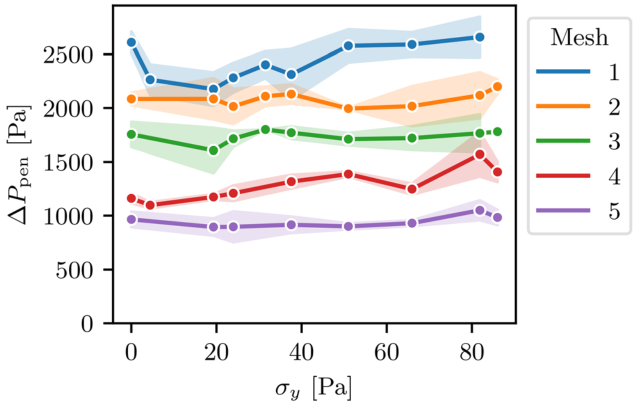

Fig. 5 Penetration pressure ΔP_{pen} as a function of yield stress σ_y, for the five meshes used. Each point represents the average value for a set of parameters (σ_y, m, e) over 2 to 10 experiments. The lighter-colored areas indicating the corresponding standard deviations.

where β is a numerical factor set by the geometry. In Fig. 6, we plot the yield-stress contribution, ΔP_{σ_y}, obtained from eqn (2), as a function of the rescaled yield stress $(e/m_{\mathrm{real}})\sigma_y$.

Although measurement uncertainties dominate, the measured ΔP_{σ_y} is somehow consistent with a minimal flow model with a geometric prefactor $\beta = 4$ (eqn (3)), comparable to other estimations in the literature.[12,13]

We note, however, that the yield-stress contribution remains one order of magnitude lower than the capillary contribution $\Delta P_{\mathrm{L,max}}$. The former scales with the yield stress, $\approx 10^2$ Pa in our case, and the latter is of the order of 10^3 Pa (Fig. 4). For the range of yield stresses and mesh geometries investigated, the effect of yield-stress on the overall threshold penetration pressure is therefore quantifiable, but marginal. In order to observe a significant effect of the yield stress on the penetration pressure, *i.e.*, $\Delta P_{\mathrm{L,max}} \sim \Delta P_{\sigma_y}$, a yield stress of at least 500–1000 Pa would have been required for mesh sizes ranging from 60 to 200 μm.

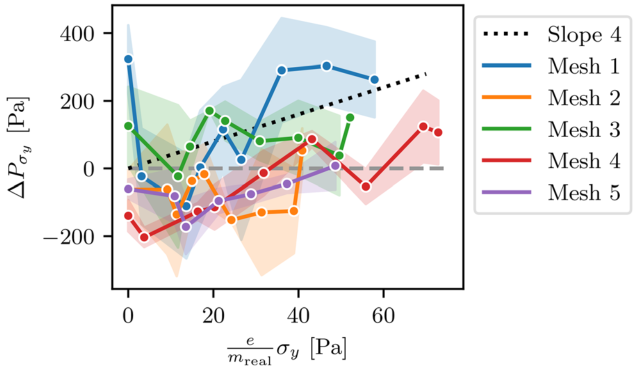

Fig. 6 Yield-stress contribution to the penetration pressure ΔP_{σ_y} as a function of the rescaled yield stress $(e/m_{\mathrm{real}})\sigma_y$, for the five mesh geometries. The dotted line corresponds to $\beta = 4$ in eqn (3). Each point represents the average value for a set of parameters (σ_y, m, e) over 2 to 10 experiments. The lighter-colored areas indicate the corresponding standard deviations.

3.2. Local penetration phenomenology is controlled by a priming pressure

3.2.1. A complex phenomenology. In contrast, the presence of a yield-stress plays a significant role in the imbibition phenomenology. On the one hand, when the yield-stress is sufficiently high, the fluid inside adjacent pores coalesce when passing through the mesh (Fig. 2 and 7a). On the other hand, in the absence of yield-stress, the fluid bursts through a single pore without touching the neighboring ones (Fig. 7b). We identify these phenomena from changes in the light reflection pattern on the fluid–air interface. When the fluid in adjacent pores merge, a lens effect makes the fibers below the fluid appear thicker (Fig. 7a). In turn, when the fluid goes through an isolated pore, the fluid–air interface becomes wider and blurry, indicating that the fluid has moved out of the focal plane (Fig. 7b).

To elucidate this transition, we investigated the penetration phenomenology of fluids with varying yield-stress values, through 5 different geometries, and gathered the results in a phase diagram (Fig. 7c). We observe that, in the absence of yield stress, the fluid systematically bursts through the mesh, regardless of the mesh geometry. Conversely, beyond a yield stress of approximately 50 Pa, the fluid systematically coalesces during penetration. At intermediate yield stress values, the geometry of the mesh plays a significant role: burst dynamics dominate in smaller pores, and coalescence prevails in larger pores. The presence of a yield stress thus combines with the pore geometry to completely alter the penetration dynamics.

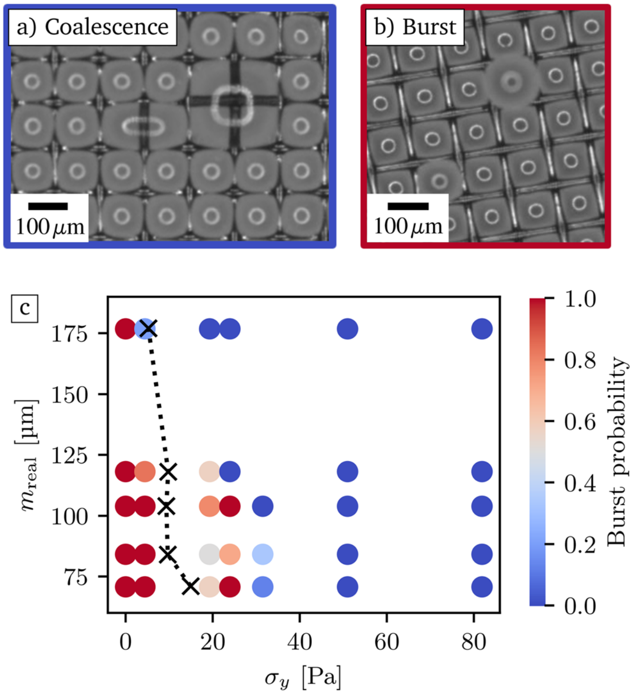

Fig. 7 Snapshots of the penetration phenomenology with mesh 2. (a) The fluid coalesces with adjacent pores as it passes through. (b) The fluid bursts through a single pore. (c) Phase diagram of the burst occurrences, as a function of the yield-stress σ_y and the pore size. Each point represents the measured burst probability. For each point, at least four videos were recorded, and up to eight videos in the transition zone where both occurrence of burst and coalescence may occur. The black crosses correspond to eqn (5), the dotted lines in between are a guide to the eye.

3.2.2. Fluid retraction controls penetration dynamics. In the previous section, we showed that the penetration pressure was largely controlled by the Laplace pressure from eqn (1): once the fluid inside a pore reaches the immersion angle α_c, at which the pressure equals the maximum Laplace pressure $\Delta P_{\mathrm{L,max}}$, it flows through the mesh. If the mesh was perfectly homogeneous, we would thus expect penetration to occur simultaneously in all the pores. The fact that the fluid instead goes through an isolated pore therefore points to the presence of mesh imperfections, such as variations in pore size or heterogeneities in surface wettability, which locally lowers the Laplace pressure.[31]

When the maximal Laplace pressure is reached in this specific pore (Fig. 8, orange square), the fluid starts flowing through it which leads to a drop in Laplace pressure (Fig. 8, orange circle). In the neighboring pores, however, the maximal Laplace pressure has not been reached (Fig. 8, blue square). We then expect two possible behaviours. Either the Laplace pressure inside the neighboring pores also drops, or it remains constant. In the former case, the fluid retracts from the neighboring pores and empties into the unstable pore. The fluid then flows through a unique pore, which corresponds to the burst scenario we observed at low yield-stress and small pore size (Fig. 7c). In the latter case, the fluid keeps advancing in the unstable pore without retracting from the neighboring ones, until they coalesce.

A closer look at the light reflection pattern around the penetration time supports this simple model of the two possible behaviours (Fig. 9). Step-by-step video analysis indeed shows how the reflection pattern reveals the interface position in each pore (Fig. 2). The pattern is square-like at low pressure, when the immersion angle α is low (Fig. 2d), and becomes circular as the interface advances through the pore (Fig. 2e). At low yield stress, as the fluid bursts through a single pore, the

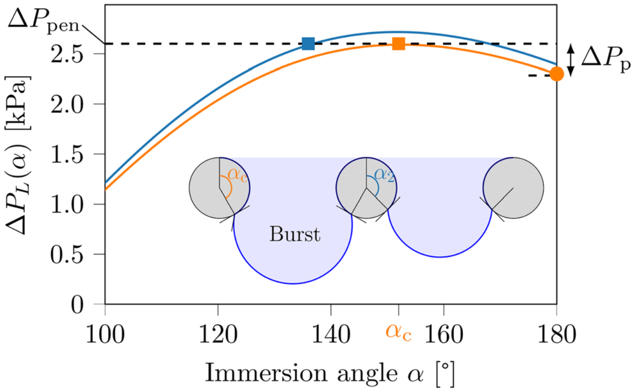

Fig. 8 Main: Laplace pressure as a function of the immersion angle for two pores differing in size or wetting properties. One of them (orange curve) is characterized by a smallest capillary pressure. Inset: Illustration of meniscus advancement in two pores with different capillary pressures. The liquid goes through the pore with the smallest maximum pressure.

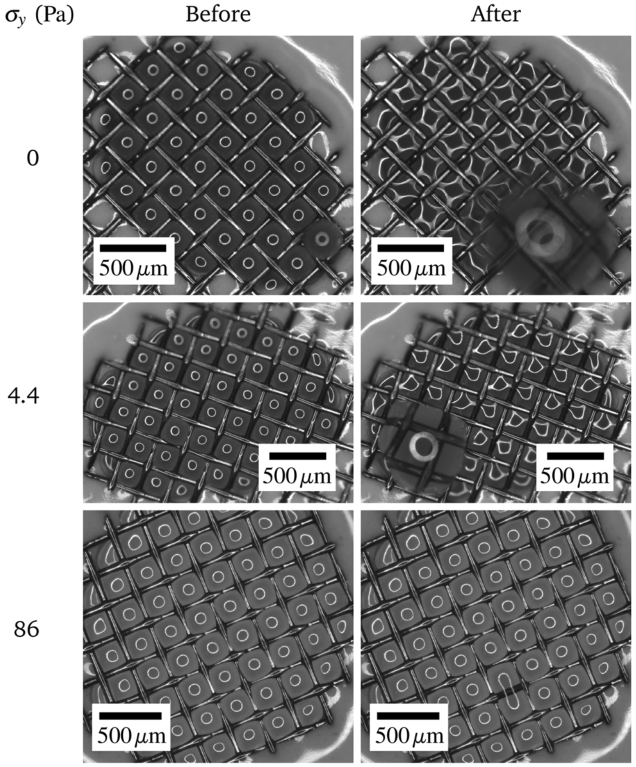

Fig. 9 Snapshots from experimental videos obtained with mesh 5 and three different yield stresses (0 Pa, 4.4 Pa, 86 Pa). Snapshots referenced as 'before' are taken just before the start of the flow and those referenced as 'after' are taken just after. The comparison of the reflection patterns between two snapshots (before/after) gives information about the existence or not of fluid retraction.

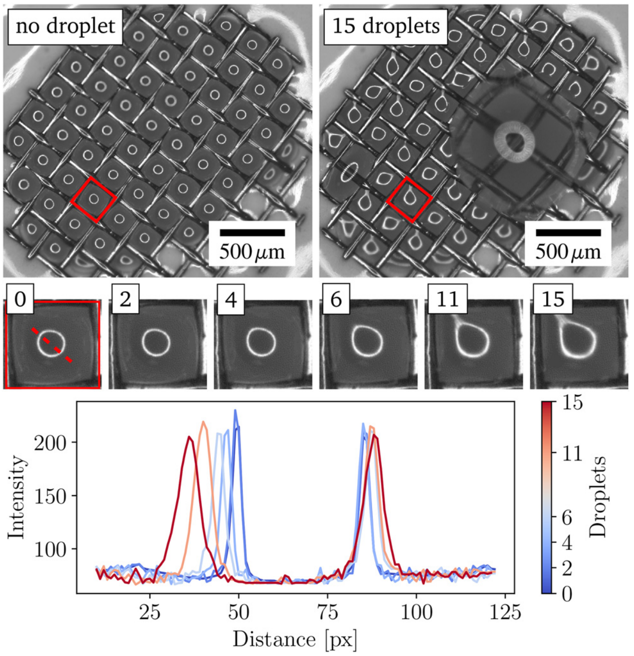

Fig. 10 Snapshots from experimental videos with mesh 5 and a fluid with a yield stress of 24 Pa, comparing fluid retraction before the first coalescence and when the coalescence cluster is formed by 15 droplets. The sequence of numbered images in the center of the figure displays the different stages of retraction in a selected pore (red square), as the coalescence cluster expands (for each image, we indicate the number of droplets in the coalescence cluster). The graph shows the evolution of light intensity along the red axis indicated in image 0 at each stage (the two peaks correspond to the edges of the white circle).

reflection pattern in neighboring pores rapidly turns back to a square-like shape, akin to the early stage of fluid advancement (Fig. 9 top). This indicates that, as the fluid flows through a pore, it simultaneously retracts in the neighboring ones. This phenomenology is reminiscent of Haines jumps that have been observed when Newtonian fluids penetrate hydrophobic porous media.[2–5,20] Conversely, when the fluid of neighboring pores coalesces at high yield stress, the reflection pattern in the rest of the mesh remains circular (Fig. 9 bottom). The progression of the fluid in each pore is therefore decoupled from that in neighboring pores. The pores do not interact and behave as if disconnected from each other. For intermediate yield stress values, although no fluid retraction is observed during the first coalescence event, retraction gradually occurs as the coalescence includes more and more neighbors (Fig. 10).

These observations are consistent with a drop of Laplace pressure, which pumps the neighbouring fluid. We thus name this pressure drop the priming pressure. As the size of the coalescent drop increases, its curvature decreases and lowers the inner Laplace pressure. The pressure difference, between the fluid in the coalescent drop and the neighboring pores, thus increases. Eventually, it becomes large enough for the fluid in the neighboring pores to empty into the coalescent drop, in other words to retract, even in the presence of a yield stress. Overall, this suggests that the penetration phenomenology is determined by a retraction process, which itself is governed by a competition between the yield stress and this priming pressure.

3.2.3. Priming pressure *vs.* yield stress.

To test this hypothesis, we further investigate the competition between yield stress and a priming pressure, which we define as the difference between the Laplace pressure at penetration $\Delta P_{\mathrm{L,max}}$, and the Laplace pressure inside the unstable pore when the immersion angle reaches coalescence:

$$\Delta P_{\mathrm{p}} = \Delta P_{\mathrm{L,max}} - \Delta P_{\mathrm{L}}(\alpha_{\mathrm{coalescence}}), \tag{4}$$

with $\alpha_{\mathrm{coalescence}} = 180°$ for a fluid-fiber contact angle $\theta = 90°$. Priming pressure ΔP_{p}, defined as such, corresponds to the maximal pressure difference between the unstable pore and an adjacent one. If this pressure is insufficient to drive fluid retraction, imbibition occurs through a coalescence process.

Assuming that the typical distance between the center of two adjacent pores is $m + d$, the resulting pressure gradient is $\nabla P_{\mathrm{p}} = \Delta P_{\mathrm{p}}/(m + d)$. In the absence of yield stress, this pressure gradient drives the fluid retraction observed in the neighboring pores and is responsible for the burst regime. In the presence of a yield stress, however, a flow can only occur if this pressure gradient overcomes ∇P_y, the pressure gradient required to advance the fluid through a pore of typical size m. In a fluid at rest, it would be equal to $4\sigma_y/m$ for a cylindrical pore of diameter m (see Section S2 for details). Here, as the fluid has already partially flowed through the pore, reverting its flowing direction implies $\nabla P_y = 8\sigma_y/m$.[29]

Following this model, fluid retraction systematically occurs when $\nabla P_p > \nabla P_y$. In other words, for a given mesh geometry, the fluid only flows from the neighboring pores into the unstable one if its yield stress σ_y is lower than the critical value

$$\sigma_{yc} = \frac{m}{8(m+d)}\Delta P_p(m, \ell), \qquad (5)$$

which depends on the mesh geometry mainly through the priming pressure. In Fig. 7c, we placed the point corresponding to $\sigma_y = \sigma_{yc}$ for each of the five mesh geometries we studied (black crosses). We note that, as predicted by our model, this criterion clearly separates the region where the probability to burst is one from the rest of the phase diagram.

This remarkable agreement demonstrates that, while the penetration pressure is set by capillary forces, the imbibition phenomenology is controlled by a tight interplay between the yield stress and a previously unreported priming pressure.

4. Conclusions

In this work, we investigated the forced imbibition of a hydrophobic mesh by a water-based yield-stress fluid, for a range of mesh geometry and yield-stress values. Combining pressure measurements and direct visualization techniques, we revealed the subtle way the yield-stress influences imbibition mechanics. First, we focused on the pressure required to force the fluid through the mesh. We measured the yield-stress contribution and showed that it was minor compared to the capillary contribution. Then, we turned to the imbibition pattern. We revealed that the manner the fluid goes through the mesh, either through a single pore or a collection of pores, is governed by an interplay between yield-stress and mesh geometry. We explained it by detailing local pressure gradients, and unveiled the existence of a priming pressure, which we used to establish a predictive criterion for the penetration pattern as a function of yield-stress.

More generally, the penetration of a fluid into a non-wetting 2D mesh is controlled by two capillary pressures: the maximum Laplace pressure $\Delta P_{L,max}$ and the priming pressure ΔP_p. The first one sets the pressure at which the penetration occurs and the second one is responsible for the penetration pattern, *i.e.*, through a single pore with a mechanism similar to Haines instability,[2–5] or homogeneously through many pores. In the case of the penetration of 2D mesh by a yield-stress fluid, these two pressures have to be compared to the yield-stress value, giving two Bingham capillary numbers,[32,33] also known as plastocapillary numbers,[34,35] $B_{c,L} = \sigma_y/\Delta P_{L,max}$ and $B_{c,p} = \sigma_y/\Delta P_p$. In the present study, $B_{c,L} \ll 1$ whereas $B_{c,p} \sim 1$, indicating that the yield stress does not affect the threshold penetration pressure but greatly influences the penetration pattern. In this regime, the yield stress is large enough to prevent Haines instability and thus ensure a more homogeneous penetration of the fluid in the porous matrix, while keeping the threshold penetration pressure almost as low as the capillarity allows. It can be considered as the optimal regime for applications seeking homogeneous penetration at minimal pressure. In this case, using a low yield stress fluid is beneficial with respect to a Newtonian fluid.

An attractive perspective of this work would be to study the penetration of a yield-stress fluid into non-wetting model porous media on microfluidic chips[3,4] or into a few 2D meshes associated in series.[20] The latter would be a first step to model the penetration of 3D fibrous porous medium by a non-wetting complex fluid. Another perspective could be to go towards industrial applications and their more specific complex fluids such as cement paste, paints and cosmetics. For instance, incorporating grains inside the yield-stress fluid would enable the exploration of the coupling between rheology, mesh geometry, grain size and solid fraction.[36]

Author contributions

M. B. designed the experimental set-up and conducted all experiments under the supervision of C. B., M. L., L. V., and N. B. M. B. analyzed the data, and C. B. developed the model to interpret it. All authors contributed equally to writing the article. Funding acquisition by C. B., M. L. and L. V.

Conflicts of interest

There are no conflicts to declare.

Data availability

Data are available at **https://doi.org/10.5281/zenodo.16412539** and include: Donnees_manip_compression_QS_sup.csv containing the experimental conditions and data for the pressure measurements; Figures_Article.ipynb, the python code that generates the figures from the experimental data; the movies showing the penetration of 2D hydrophobic meshes by water-based fluids (fig2.avi, fig7a.avi, fig7b.avi, fig9_0Pa.avi, fig9_4-p4Pa.avi, fig9_86Pa.avi, fig10) from which images shown in the Figures have been extracted; intensity profiles (goutte_0.csv, goutte_1.csv to goutte_6.csv) used to plot the graph in Fig. 10; figures (pdf files).

The data supporting this article have been included as part of the supplementary information (SI). Supplementary information is available. The supplementary Information (SI) provides details on the 2D hydrophobic meshes, the experimental protocol, the pressure determination, the sample preparation, the rheological characterization, and the contact angle measurement. See DOI: **https://doi.org/10.1039/d5sm00759c**.

Acknowledgements

The authors acknowledge Saint-Gobain Research for financial support, in particular the CIFRE grant of Manon Bourgade. The authors also thank Gilles Simon and Matthieu Mercury for technical support, and Solenn Moro, Julie Godefroid and Paul Jacquet for fruitful discussions. The authors thank Changwoo Bae and Anne-Laure Biance for their set up and assistance in measuring the microscopic contact angles.

References

1 Y. Deng, Y. Chen, J. Zhi, W. Yang and Y. Li, *Capillarity*, 2024, **13**, 60–67.
2 W. B. Haines, *J. Agric. Sci.*, 1930, **20**, 97–116.
3 R. T. Armstrong and S. Berg, *Phys. Rev. E*, 2013, **88**, 043010.
4 F. Moebius and D. Or, *J. Colloid Interface Sci.*, 2012, **377**, 406–415.
5 Z. Sun and J. C. Santamarina, *Phys. Rev. E*, 2019, **100**, 023115.
6 D. Bonn, M. M. Denn, L. Berthier, T. Divoux and S. Manneville, *Rev. Mod. Phys.*, 2017, **89**, 035005.
7 R. L. J. Peek and D. A. McLean, *Ind. Eng. Chem., Anal. Ed.*, 1934, **6**, 85–90.
8 K. Ghali, B. Jones and J. Tracy, *Text. Res. J.*, 1994, **64**, 106–111.
9 I. Pezron, G. Bourgain and D. Quéré, *J. Colloid Interface Sci.*, 1995, **173**, 319–327.
10 E. Ezzatneshan and R. Goharimehr, *Phys. Fluids*, 2020, **32**, 113303.
11 C. Duprat, *Annu. Rev. Fluid Mech.*, 2022, **54**, 443–467.
12 T. Chevalier, C. Chevalier, X. Clain, J. Dupla, J. Canou, S. Rodts and P. Coussot, *J. Non-Newtonian Fluid Mech.*, 2013, **195**, 57–66.
13 S. Shahsavari and G. H. McKinley, *J. Non-Newtonian Fluid Mech.*, 2016, **235**, 76–82.
14 D. Bauer, L. Talon, Y. Peysson, H. B. Ly, G. Batot, T. Chevalier and M. Fleury, *Phys. Rev. Fluids*, 2019, **4**, 063301.
15 E. Chaparian, *J. Fluid Mech.*, 2024, **980**, A14.
16 E. Chaparian, *Phys. Fluids*, 2025, **10**, 093301.
17 B. C. Blackwell, A. E. Nadhan and R. H. Ewoldt, *J. Non-Newtonian Fluid Mech.*, 2016, **238**, 107–114.
18 Y. Zong, A. Oron, H. Liu and Y. Jiang, *Langmuir*, 2023, **39**, 9808–9815.
19 S. M. Lee, D. J. Oh, I. D. Jung, P. G. Jung, K. H. Chung, W. I. Jang and J. S. Ko, *J. Micromech. Microeng.*, 2009, **19**, 125024.
20 M. Jamali, H. Vahedi Tafreshi and B. Pourdeyhimi, *J. Appl. Phys.*, 2019, **125**, 145304.
21 A. Delbos, PhD thesis, Université Paris-Est, 2010.
22 G. Zhang, M. A. Quetzeri-Santiago, C. A. Stone, L. Botto and J. R. Castrejón-Pita, *Soft Matter*, 2018, **14**, 8182–8190.
23 C. Bae, S. Oh, J. Han, Y. Nam and C. Lee, *Soft Matter*, 2020, **16**, 6072–6081.
24 S. Ryu, P. Sen, Y. Nam and C. Lee, *Phys. Rev. Lett.*, 2017, **118**, 014501.
25 A. Abouei Mehrizi, S. Lin, L. Sun and L. Chen, *Langmuir*, 2022, **38**, 6106–6115.
26 G. Ovarlez, S. Cohen-Addad, K. Krishan, J. Goyon and P. Coussot, *J. Non-Newtonian Fluid Mech.*, 2013, **193**, 68–79.
27 Z. Jaworski, T. Spychaj, A. Story and G. Story, *Rev. Chem. Eng.*, 2022, **38**, 881–919.
28 A. Stalder, G. Kulik, D. Sage, L. Barbieri and P. Hoffmann, *Colloids Surf., A*, 2006, **286**, 92–103.
29 L. Jørgensen, M. Le Merrer, H. Delanoë-Ayari and C. Barentin, *Soft Matter*, 2015, **11**, 5111–5121.
30 J. Boujlel and P. Coussot, *Soft Matter*, 2013, **9**, 5898–5908.
31 Y. Xiao, B. Li, C. Wei, A. Oron and Y. Jiang, *J. Colloid Interface Sci.*, 2025, 137810.
32 V. Bertola, *J. Phys.: Condens. Matter*, 2008, **21**, 035107.
33 G. Martouzet, L. Jørgensen, Y. Pelet, A.-L. Biance and C. Barentin, *Phys. Rev. Fluids*, 2021, **6**, 044006.
34 V. Sanjay, D. Lohse and M. Jalaal, *J. Fluid Mech.*, 2021, **922**, A2.
35 M. Jalaal, B. Stoeber and N. J. Balmforth, *J. Fluid Mech.*, 2021, **914**, A21.
36 N. Roussel, T. L. H. Nguyen and P. Coussot, *Phys. Rev. Lett.*, 2007, **98**, 114502.